PCCP

PAPER

View Article Online
View Journal | View Issue

Cite this: *Phys. Chem. Chem. Phys.*, 2016, **18**, 20640

Homogeneity and elemental distribution in self-assembled bimetallic Pd–Pt aerogels prepared by a spontaneous one-step gelation process

M. Oezaslan,*[ab] W. Liu,[c] M. Nachtegaal,[a] A. I. Frenkel,[d] B. Rutkowski,[e] M. Werheid,[c] A.-K. Herrmann,[c] C. Laugier-Bonnaud,†[a] H.-C. Yilmaz,‡[a] N. Gaponik,[c] A. Czyrska-Filemonowicz,[e] A. Eychmüller[c] and T. J. Schmidt*[af]

Multi-metallic aerogels have recently emerged as a novel and promising class of unsupported electrocatalyst materials due to their high catalytic activity and improved durability for various electrochemical reactions. Aerogels can be prepared by a spontaneous one-step gelation process, where the chemical co-reduction of metal precursors and the prompt formation of nanochain-containing hydrogels, as a preliminary stage for the preparation of aerogels, take place. However, detailed knowledge about the homogeneity and chemical distribution of these three-dimensional Pd–Pt aerogels at the nano-scale as well as at the macro-scale is still unclear. Therefore, we used a combination of spectroscopic and microscopic techniques to obtain a better insight into the structure and elemental distribution of the various Pd-rich Pd–Pt aerogels prepared by the spontaneous one-step gelation process. Synchrotron-based extended X-ray absorption fine structure (EXAFS) spectroscopy and high-angle annular dark-field (HAADF) scanning transmission electron microscopy (STEM) in combination with energy-dispersive X-ray spectroscopy (EDX) were employed in this work to uncover the structural architecture and chemical composition of the various Pd-rich Pd–Pt aerogels over a broad length range. The $Pd_{80}Pt_{20}$, $Pd_{60}Pt_{40}$ and $Pd_{50}Pt_{50}$ aerogels showed heterogeneity in the chemical distribution of the Pt and Pd atoms inside the macroscopic nanochain-network. The features of mono-metallic clusters were not detected by EXAFS or STEM-EDX, indicating alloyed nanoparticles. However, the local chemical composition of the Pd–Pt alloys strongly varied along the nanochains and thus within a single aerogel. To determine the electrochemically active surface area (ECSA) of the Pd–Pt aerogels for application in electrocatalysis, we used the electrochemical CO stripping method. Due to their high porosity and extended network structure, the resulting values of the ECSA for the Pd–Pt aerogels were higher than that for a commercially available unsupported Pt black catalyst. We show that the Pd–Pt aerogels possess a high utilization of catalytically active centers for electrocatalytic applications based on the nanostructured bimetallic framework. Knowledge about the homogeneity and chemical distribution of the bimetallic aerogels can help to further optimize their preparation by the spontaneous one-step gelation process and to tune their electrocatalytic reactivity.

Received 23rd May 2016,
Accepted 1st July 2016

DOI: 10.1039/c6cp03527b

www.rsc.org/pccp

1. Introduction

Multi-metallic self-assembled materials that combine the physical, chemical and catalytic properties of nanomaterials with those of macroscopic materials are of large interest for academia and industry. They offer great potential for various applications in heterogeneous catalysis and electrochemistry. In particular, multi-metallic aerogels consisting of well-connected nanochains are excellent self-assembled nanomaterials with unique physical, chemical and (electro)catalytic properties.[1–7] They form an immense framework over a large length scale and show lower densities, higher porosities and larger surface areas than other unsupported metallic materials.[1,4,8–10] In the last few years,

[a] *Paul Scherrer Institut, CH-5232 Villigen PSI, Switzerland. E-mail: mehtap.oezaslan@uni-oldenburg.de, thomasjustus.schmidt@psi.ch*
[b] *Physical Chemistry, Carl von Ossietzky University of Oldenburg, 26111 Oldenburg, Germany*
[c] *Physical Chemistry, TU Dresden, Bergstrasse 66b, 01062 Dresden, Germany*
[d] *Department of Physics, Yeshiva University, 245 Lexington Avenue, New York, New York 10016, USA*
[e] *International Centre of Electron Microscopy for Material Science and Faculty of Metals Engineering and Industrial Computer Science, AGH University of Science and Technology, Al. A. Mickiewicza 30, 30-059 Kraków, Poland*
[f] *Laboratory of Physical Chemistry, ETH Zürich, 8093 Zürich, Switzerland*
† Present address: Laboratoire d'Electrochimie et de Physico-chimie des Matériaux et des Interfaces, 38400 St Martin d'Hères, France.
‡ Present address: Laboratory of Inorganic Chemistry, ETH Zurich, 8093 Zurich, Switzerland.

two synthetic approaches for the preparation of various mono- and multi-metallic aerogels have been developed: (1) a two-step gelation process[4] and (2) a spontaneous one-step gelation process.[2,3] The first one includes two independent synthetic steps, namely the formation of metallic nanoparticles and the subsequent growth of hydrogels in aqueous solutions by connecting and linking the nanoparticles. In contrast, in the spontaneous one-step gelation process, the metal precursors are chemically reduced and form a hydrogel spontaneously. Hydrogels are the pre-stage for the preparation of metallic aerogels. Careful removal of the solvent from the gel without significant loss of porosity and structure takes place by supercritical CO_2 drying. In both synthetic approaches, the gelation process still remains the very critical step for the preparation of homogeneous multi-metallic aerogels. For both synthetic routes the formation mechanisms of these aerogels have been unclear to date, since gelation is a highly complex process. Very recently, AuPt nanowires have been prepared with a similar structure and morphology like the present aerogels in this work.[11] The authors suggested that the formed hydrogen bubbles obtained by the decomposition of $NaBH_4$ serve as a dynamic template to prepare the connected AuPt nanowires. The postulated mechanism introduces the anchor and growth of the initially formed AuPt nuclei on the surface and interspaces of these hydrogen bubbles to form a three-dimensional network structure.

The electrocatalytic properties of multi-metallic materials strongly differ from those of their mono-metallic counterparts.[12–16] In particular, Pt-based alloy nanomaterials show higher reactivity and durability for the prominent electrochemical oxygen reduction reaction (ORR; $O_2 + 4H^+ + 4e^- \rightarrow 2H_2O$) which takes place at the cathode of polymer electrolyte fuel cells (PEFCs) compared to pure Pt catalysts.[12,17–27] Improvements in catalytic activity and durability at reduced material costs for Pt-based catalysts are necessary for the large-scale commercialization of PEFCs. The improved reactivity for the ORR likely originates from ensemble effects,[28] electronic effects[29,30] and geometric effects[29,30] induced by alloying of Pt.

Recently, Pd–Pt aerogels prepared by the spontaneous one-step gelation process have emerged as promising unsupported electrocatalysts with high reactivity and improved durability for the ORR.[3] The improved ORR performance is based on the large inner surface area, high porosity and the presence of a bimetallic arrangement by mixing of Pt and Pd atoms. At that time, the characteristic mixing behavior and the elemental distribution of Pd and Pt inside the different macroscopic aerogel networks were unclear. In particular, assessing the uniformity of the structure and chemical composition of self-assembled materials is a great challenge. Pure Pd, Pt and Pd–Pt systems exhibit the same crystal structures (face-centered cubic (fcc) crystal structure with the space group of $Fm\bar{3}m$) and the lattice parameters of pure Pt and Pd metals are very similar (obtained from the Inorganic Crystal Structure Database (ICSD), 3.8870 Å, for Pd and 3.9250 Å for Pt, respectively). Moreover, the mean crystallite sizes of the Pd–Pt aerogels are in the range of a few nanometers and result in broad reflections. Due to the similar lattice parameters of these dissimilar metals and the very broad reflections, crystal structure refinements by using Rietveld analysis for the identification of the single crystal phases are extremely difficult for these materials.

In addition, the electrochemically active surface area (ECSA) of Pt-based materials in today's fuel cell research is commonly determined by the under-potentially deposited hydrogen (H_{upd}) method. However if the investigated materials contain palladium, the H_{upd} method leads to an overestimation of the electrochemically active surface area (ECSA) due to hydride formation. The absorption of hydrogen leads to the lattice expansion of Pd and can even create fractures of the nanomaterials or H_2 embrittlement[31,32] due to the formation of hydrogen sub-surface layers. A more accurate method to determine the ECSA of Pd-based material systems is the here presented CO stripping method.

In this work, we present detailed information about the structural and chemical architectures of various Pd-rich aerogels prepared by the spontaneous one-step gelation process. Knowledge about the structure and chemical composition of these highly complex Pd–Pt aerogels helps to better understand the experimentally observed ORR activity. Compared to our previously published work on bimetallic Pd–Pt aerogels,[1,3] we carefully investigated the ECSA of pristine $Pd_{80}Pt_{20}$, $Pd_{60}Pt_{40}$ and $Pd_{50}Pt_{50}$ aerogels by using the CO stripping method. Based on the microscopic and spectroscopic results, we can conclude that the bimetallic aerogels are largely alloyed; however, the chemical composition of the aerogels strongly varies along the nanochains. Altogether, the aerogels exhibit good homogeneity at the atomic scale, however their chemical composition significantly varies along the larger-scale nanochains and thus in the entire aerogel framework.

2. Experimental part

2.1 Synthesis of various bimetallic Pd–Pt aerogels

Potassium tetrachloropalladate(II) (K_2PdCl_4) (99.99%) and chloroplatinic(IV) acid hydrate (H_2PtCl_6) (99.995%) were used as metal precursor salts (supplied by Sigma Aldrich). The formation of the Pd–Pt hydrogel took place spontaneously by the simultaneous reduction of both metal precursor salts with $NaBH_4$ (96%, supplied by Fluka) in one pot. The desired ratios of Pd : Pt can be adjusted by changing the atomic ratio of the metal precursors in the reaction solution. More details about the synthesis of Pd–Pt aerogels by the spontaneous one-step gelation process can be found elsewhere.[1–3] As an example, for the preparation of $Pd_{50}Pt_{50}$ aerogels, each metal precursor salt was separately dissolved in purified water. The final concentrations were 10 mM and 0.24 mM for K_2PdCl_4 and H_2PtCl_6, respectively. 4 ml of 10 mM K_2PdCl_4 and 167 μl of 0.24 M H_2PtCl_6 were added in 391 ml of purified water. The light yellow solution was then stirred for about 10 min. Afterwards, 4.5 ml of freshly prepared 40 mM $NaBH_4$ solution was rapidly added to the solution. A quick color change from light yellow to dark brown was observed. The dark brown reaction solution was stirred for another 30 minutes and then divided into four 100 ml vials and subsequently left to settle at room temperature. After around 3 days, a black hydrogel

formed and precipitated at the bottom of the vials. It was washed with water 6–8 times by exchanging half the volume of the supernatant. Then, the hydrogels were transferred to 10 ml vials, and acetone was dropwise added to the supernatant. The amount of acetone in the supernatant was stepwise increased to largely exchange the water. Subsequently, the hydrogel was stored in a desiccator containing dry acetone with calcium chloride. To remove the residual acetone, the desiccator was evacuated by applying vacuum overnight. The acetone washing and vacuum-drying process were repeated several times to remove trace amounts of water in the gel. Finally, the acetone-containing gel was dried under supercritical CO_2 conditions to minimize shrinkage and collapsing of the aerogel framework. After critical CO_2 drying, the resulting aerogel was a black monolith.

2.2 Structural characterization

2.2.1 Transmission electron microscopy (TEM). The morphology and the mean diameter of the nanochains were established by using TEM. A FEI TECNAI T20 microscope with a LaB_6 cathode was operated at an accelerating voltage of 200 kV. The mean diameters of the nanochains of the various Pd–Pt aerogels were determined by measuring more than 100 regions of the nanochain segments of the aerogel framework using ImageJ.

2.2.2 Scanning transmission electron microscopy (STEM) equipped with energy-dispersive X-ray spectroscopy (EDX). High-angle annular dark-field (HAADF) STEM-EDX investigations were performed on a probe Cs corrected Titan3 G2 60–300 analytical electron microscope, equipped with the ChemiSTEM system for fast EDX acquisition and high-brightness X-FEG electron source in combination with the 4 windowless silicon drift detectors (Super X). In order to avoid or at least minimize sample damage or to influence the measurements of the elemental distribution, the EDX maps were acquired at an acceleration voltage of 60 kV and a beam current of about 150 pA (spot size 6). The acquisition time of around 2 h allows collecting enough signal for proper background subtraction and quantification using L_α lines of Pd and Pt.

2.2.3 Extended X-ray absorption fine structure (EXAFS) spectroscopy. EXAFS measurements on various Pd–Pt aerogels were carried out at the Swiss Light Source (SLS), Switzerland, using the SuperXAS beamline. The storage ring of the SLS was operated at a beam current of 400 mA and the storage ring energy was 2.4 GeV. To detect the incident (I_0) and transmitted (I_1 and I_2) X-ray intensities, ionization chambers with lengths of 15 and 30 cm were filled with Ar for the Pd K-edge measurements. In the case of Pt L_3-edge measurements the ionization chambers were filled with N_2. A channel-cut Si(111) crystal monochromator was employed to scan the X-ray energy from −150 eV to 1200 eV relative to the Pt L_3-edge (11.564 eV) and from −150 eV to 1200 eV relative to the Pd K-edge (24.350 eV). All EXAFS spectra at the Pt L_3- and Pd K-edges were recorded in transmission mode. The signal-to-noise ratio was improved by averaging at least three scans per sample. The averaged EXAFS spectra were then analyzed by using the IFEFFIT software suite.[33] After background subtraction and edge-step normalization of the data, the energy units (eV) were converted to photoelectron wave vector k units ($Å^{-1}$) by assigning the photoelectron energy origin, E_0, corresponding to $k = 0$, to the first inflection point of the absorption edge. The resulting $\chi(k)$ functions were weighted with k^2 to compensate for the dampening of the XAFS amplitude with increasing k. Subsequently, the EXAFS spectra were Fourier-transformed to obtain pseudo radial structure functions (RSFs).

The amplitude reduction factors ($S_0{}^2$) were obtained from the fits of the EXAFS spectra of Pd and Pt foils to be 0.91 and 0.83 for Pd and Pt, respectively. During the analysis of the Pd–Pt aerogel EXAFS spectra, the $S_0{}^2$ corresponding to each absorption edge were fixed to these values. The theoretical scattering paths for the nearest neighbor metal–metal pairs (Pt–Pt, Pd–Pd, Pt–Pd and Pd–Pt) were calculated using FEFF6[33] code on the face-centered cubic (fcc) structures of pure metals (Pt or Pd), where hetero-metallic pairs (Pt–Pd and Pd–Pt) were constructed by substituting the atoms of one type by the opposite type in the first nearest neighbor sites around the absorbing atoms. The coordination number (N), interatomic bond length (R), mean squared bond length disorder (σ^2) and correction to the energy origin (ΔE_0), together with their error bars were determined for each scattering path by fitting theoretical scattering paths to the pseudo radial distribution functions using Artemis software.[33]

The aerogel powders were mixed with cellulose as a binder and pressed into a pellet. EXAFS spectra recorded at the Pt L_3-edge and Pd K-edge for each aerogel sample were concurrently analyzed by applying several constraints between global variables in the fitting process, in order to reduce the number of variables and to increase confidence in the results. In the multi-edge EXAFS fit analysis, the distances and their disorder parameters for hetero-metallic pairs (Pd–Pt or Pt–Pd) were constrained to be equal, referred to as R(Pd–Pt) = R(Pt–Pd) and σ^2(Pd–Pt) = σ^2(Pt–Pd). Only the coordination numbers of the hetero- and homo-metallic bonds and the correction-of-edge energy (ΔE_0) for each edge were varied.

2.2 Electrochemical characterization

2.2.1 Preparation of the working electrode (WE). A dispersion of aerogel powder (1–2 mg), purified water (3.98 ml), iso-propanol (1.00 ml) and Nafion (20 μl of 5 wt% stock solution) was prepared and sonicated for 30 min. by using a horn-sonicator (supplied by Hielscher UP200H, Germany). 10 μl of the aerogel dispersion was dropped onto a clean and mirror-like surface of a glassy carbon (GC) electrode (geometric surface area of 0.196 cm^{-2}) (supplied by PINE, USA) and dried for around 20 min at 40 °C in air. The polishing procedure of the surface of the GC electrode was performed by using a 0.3 μm and then a 0.05 μm Al_2O_3 suspension with a Microcloth polishing paper (supplied by Prüfmaschine AG, Switzerland). The polished GC electrodes were alternately cleaned in water and iso-propanol. The calculated total metal loading was in the range of 10–20 $\mu g_{metal}\ cm_{geometric}{}^{-2}$.

2.3.2 Electrochemical set-up. Electrochemical experiments were performed by using the thin-film rotating disc electrode (RDE) technique[34,35] equipped with a rotator (supplied by PINE, USA) and a potentiostat (Biologic, France). A home-made three-compartment electrochemical glass cell contained a gold wire

as a counter-electrode and a mercury–mercury sulfate electrode (supplied by Biologic, France) as a reference electrode and a thin-film coated GC electrode (WE). The reference electrode was positioned with a Luggin–Haber capillary close to the WE. The glass cell was cleaned by immersing into a "piranha" solution (mixture of 3/4 H_2SO_4 (96–98%) and 1/4 H_2O_2 (30%)) overnight. Afterwards, the cell was washed with purified water several times. 0.1 M $HClO_4$ was used as an electrolyte and was freshly prepared by dilution of 70% suprapure $HClO_4$ (supplied by VWR). The purity of the used gases, nitrogen and carbon monoxide (supplied by Messer), was 5.0 and 4.5, respectively.

2.3.3 Determination of the electrochemically active surface area (ECSA). The electrochemically active surface area (ECSA) of the Pd–Pt aerogels was determined by electrochemical oxidation of a pre-adsorbed monolayer of CO, referred to as CO stripping. The WE was immersed into the electrolyte under potential control and at a rotation speed of 1600 rpm (rotations per minute). During the saturation of the electrolyte with CO for 8 min, the WE was held at 0.1 V per RHE. Afterwards, the excess dissolved CO from the electrolyte was removed by bubbling with N_2 through the electrolyte for around 25 min. Three CV profiles were acquired with a scan rate of 50 mV s^{-1} in a potential range of 0.35–1.2 V per RHE. To consider the contribution of adsorbed anions (OH^-, ClO_4^-) on the aerogel surface in this potential range, the first CV profile was subtracted from the second CV profile. After subtraction the ECSA was established by integrating the anodic CO stripping current peak assuming a charge of 415 μC cm_{real}^{-2} for the $Pd_{50}Pt_{50}$ aerogel to oxidize one CO monolayer. The values for the other Pd–Pt aerogels are a weighted average between the pseudo-capacities of pure Pt[36] (420 μC cm^{-2}) and Pd[37] (410 μC cm^{-2}) surfaces.

Throughout the paper, all potentials are given with respect to the reversible hydrogen electrode (RHE).

3 Results and discussion

3.1 Structural characterization of the Pd-rich Pd–Pt aerogels

Structural investigations of the pristine $Pd_{80}Pt_{20}$, $Pd_{60}Pt_{40}$ and $Pd_{50}Pt_{50}$ aerogels with various chemical compositions were carried out by EXAFS spectroscopy, (S)TEM and EDX to obtain deeper insights into the chemical distribution and structural homogeneity of the unsupported three-dimensional bimetallic frameworks at different length scales. The structural results obtained from each technique will be summarized and discussed in the next sections.

3.1.1 Transmission electron microscopy (TEM). TEM measurements were performed on the various Pd–Pt aerogels to investigate their morphology and mean diameter of the nanochain segments. The TEM micrographs of representative regions of the $Pd_{80}Pt_{20}$, $Pd_{60}Pt_{40}$ and $Pd_{50}Pt_{50}$ aerogels at low and high magnifications are shown in Fig. 1. At low magnification, the TEM micrographs display the connection and linking of the nanochains to form the aerogel framework over a large length scale. Due to the high degree of cross-linked nanochains, the aerogels are entirely self-assembled and form a three-dimensional macroscopic network with high porosity and large inner surface area. Nitrogen physisorption results confirmed the large surface areas of the unsupported Pd–Pt aerogels.[1,3] The Brunauer–Emmett–Teller (BET) values of these aerogel materials are in the range of 60 and 80 $m^2\ g^{-1}$. Detailed information about the structure of the nanochains is presented in the TEM micrographs at higher magnification in Fig. 1. The mean diameters of the nanochains are 4.0 ± 1.4 nm, 4.3 ± 1.2 nm and 4.2 ± 1.2 nm for the $Pd_{80}Pt_{20}$, $Pd_{60}Pt_{40}$ and $Pd_{50}Pt_{50}$ aerogels, respectively. The dark contrast features seen in the TEM micrographs of the various Pd–Pt aerogels signify the overlapping of the nanochains or a certain extent of agglomeration in these regions. Other contrast features based on the atomic numbers of dissimilar atoms within the nanochains are not obvious. Since the lattice parameters of Pd and Pt, having a face-centered cubic (fcc) structure, are very close to each other (388.70 pm and 392.50 pm for Pd and for Pt obtained from the ICDD[38]), a discrimination by determining the atomic distances of lattice planes from the high-resolution TEM micrographs is not meaningful.

Based on the TEM results we can conclude that all Pd–Pt aerogels prepared by the spontaneous one-step gelation process show a unique macroscopic metal framework by cross-linking of nanochains to form high porosity and a large inner surface.

3.1.2 Extended X-ray absorption fine structure (EXAFS) spectroscopy. EXAFS investigations were performed on the as-prepared $Pd_{80}Pt_{20}$, $Pd_{60}Pt_{40}$ and $Pd_{50}Pt_{50}$ aerogels to provide more insights into the local homogeneity. Fig. 2 shows the k^2-weighted EXAFS spectra of the pristine Pd–Pt aerogels. Pure Pt and Pd foils were used as reference materials and the respective k^2-weighted EXAFS spectra at each edge are also plotted in Fig. 2. The comparison between k^2-weighted EXAFS spectra of the Pd–Pt aerogels and of the pure metal foils shows visible phase and amplitude differences in their $\chi(k)$ functions, indicating an atomic-level mixture of Pd and Pt atoms inside the materials.

We used a multi-edge EXAFS fit analysis of the Fourier-transformed EXAFS spectra to reduce the number of fitting variables and thus lower the error bars in the fit variables. The fitting parameters were varied for each theoretical contribution corresponding to each absorption edge concurrently, as described above.

Fig. 3 shows the Fourier-transformed k^2-weighted EXAFS spectra (shown in black solid lines) measured at both edges and the corresponding fits (denoted with red solid lines) for the as-prepared $Pd_{80}Pt_{20}$, $Pd_{60}Pt_{40}$ and $Pd_{50}Pt_{50}$ aerogels. By fitting of the EXAFS spectra, we determined the partial coordination numbers (N_{Pd-Pd}, N_{Pd-Pt}, N_{Pt-Pd} and N_{Pt-Pt}) of the absorbing atom, Pt or Pd. Table 1 summarizes the best fit parameters from the multi-edge EXAFS fit analysis. The EXAFS results obtained from both edges (Table 1) for all Pd–Pt aerogels revealed that Pt as well as Pd atoms are present in the nearest coordination shell, indicating a hetero-metallic Pt–Pd bond. Apart from the hetero-metallic Pd–Pt bond, the presence of homo-metallic bonds of Pd–Pd and Pt–Pt was also identified.

3.1.3 Total coordination numbers, chemical compositions and Cowley short range order parameters established by EXAFS. To provide more information about the chemical distribution of dissimilar atoms for the various bimetallic aerogels obtained

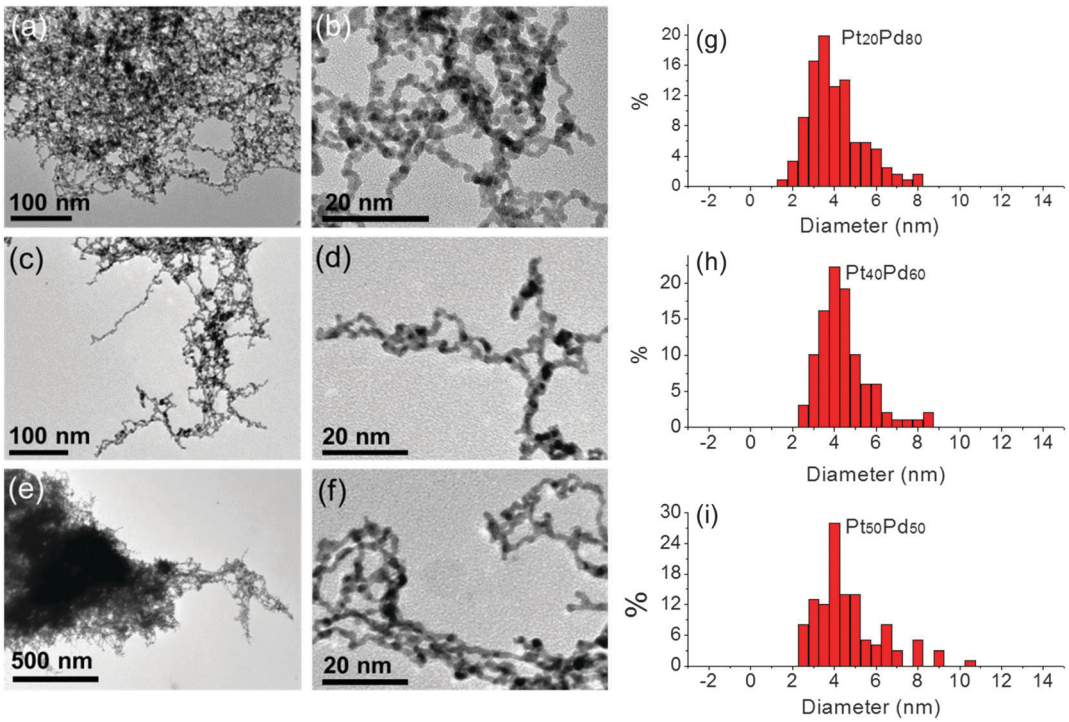

Fig. 1 TEM micrographs of the $Pd_{80}Pt_{20}$ (a and b), $Pd_{60}Pt_{40}$ (c and d) and $Pd_{50}Pt_{50}$ (e and f) aerogels at different magnifications. (g–i) Diagrams of the nanochain diameter distributions for each Pd–Pt aerogel were established by measuring more than 100 regions of the nanochain segments. The mean diameters of the nanochains are 4.0 ± 1.4 nm, 4.3 ± 1.2 nm and 4.2 ± 1.2 nm for the $Pd_{80}Pt_{20}$, $Pd_{60}Pt_{40}$ and $Pd_{50}Pt_{50}$ aerogels, respectively.

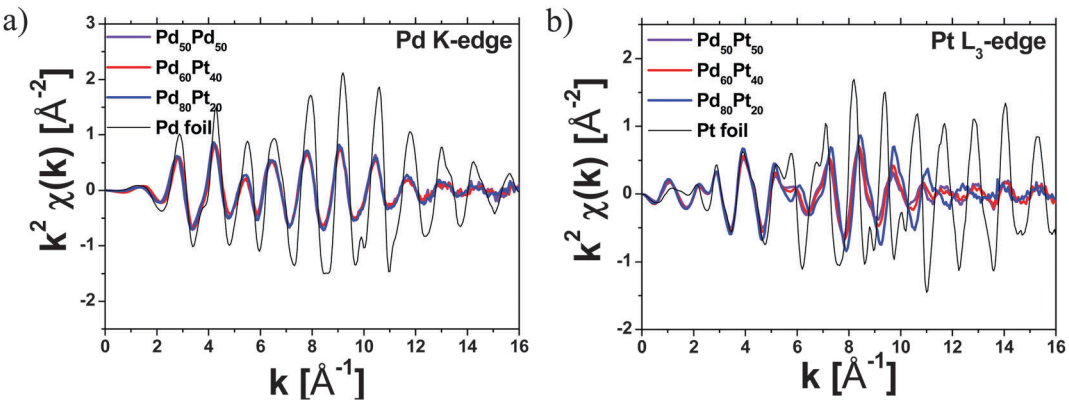

Fig. 2 k^2-weighted EXAFS data for the $Pd_{50}Pt_{50}$ (purple line), $Pd_{60}Pt_{40}$ (red line), $Pd_{80}Pt_{20}$ (blue line) aerogels and for the Pt or Pd foil (thin black line) measured at the (a) Pd K-edge and (b) Pt L_3-edge, respectively.

from the EXAFS analysis, the total coordination numbers, the atomic ratios of Pt : Pd based on the partial coordination numbers of the hetero-metallic bond and the Cowley short range order parameters could be used as additional descriptors. We want to emphasize that EXAFS is a bulk-averaging technique and the investigated local region and thus the arrangement or ordering of dissimilar atoms are representative of the entire bimetallic system. However, due to the small primary particle diameters (around 4 nm, see above), significant contribution from the aerogel surfaces can be expected. In the case of strong variations of chemical composition inside the bimetallic system, the interpretation of the EXAFS data becomes challenging.[39–41]

The total coordination numbers of each metal (N_{Pd-M} and N_{Pt-M}) in the first shell are the sum of the respective partial coordination numbers ($N_{Pd-M} = N_{Pd-Pd} + N_{Pd-Pt}$ and $N_{Pt-M} = N_{Pt-Pt} + N_{Pt-Pd}$). Table 2 shows the resulting total coordination numbers (N_{Pd-M} and N_{Pt-M}) in the first shell obtained from the EXAFS analysis at both edges of each Pd–Pt aerogel. It is noted that the values of the total coordination numbers (N_{Pd-M} and N_{Pt-M}) were around 9–10 and therefore significantly smaller than 12 which is expected for bulk fcc metal. Since the total coordination numbers were clearly below 12, all Pd–Pt aerogels possess a relatively high contribution of surface atoms compared to bulk atoms that are typical for nanoparticles. Similar coordination

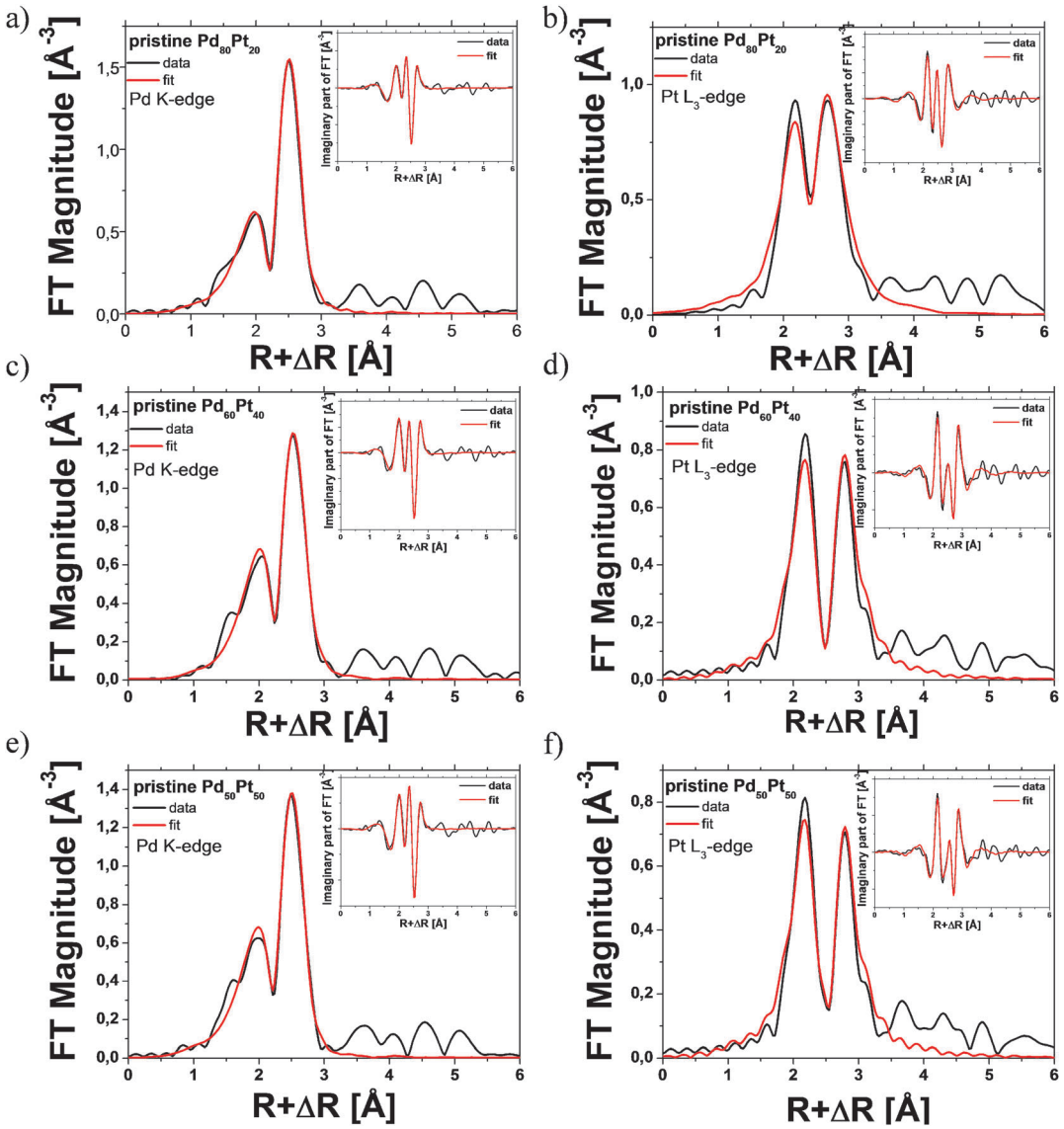

Fig. 3 Fourier-transform magnitudes of the k^2-weighted EXAFS data (black line) and of the corresponding fit (red line) at the Pd K-edge (left side) and the Pt L_3-edge (right side) for the (a and b) $Pd_{80}Pt_{20}$, (c and d) $Pd_{60}Pt_{40}$ and (e and f) $Pd_{50}Pt_{50}$ aerogels. The inset plots (b, d and f) show the imaginary part of the k^2-weighted Fourier transformed EXAFS spectra (black lines) and the corresponding fits (red lines). The k-ranges for the Fourier-transformed spectra at the Pd K-edge and the Pt L_3-edge were from 3 to 15 $Å^{-1}$ and from 3 to 14 $Å^{-1}$ for the Pd K-edge and the Pt L_3-edge, respectively, while the ranges for the fits were from 1.6 to 3.1 Å and 1.8 to 3.2 Å for the Pd K-edge and the Pt L_3-edge, respectively.

numbers indicate that the mean diameters of the nanochains for all aerogels were similar. This observation is in agreement with the results of the mean diameter of the nanochains obtained from the TEM investigations on the Pd–Pt aerogels (Fig. 1). The direct comparison between N_{Pd-M} and N_{Pt-M} of each Pd–Pt aerogel showed no significant difference, indicating that Pd and Pt atoms are randomly distributed inside the nanochains. The presence of a core–shell-type structure where one metal is predominantly in the core and the other on the surface is therefore very unlikely. This conclusion is derived from the fact that in general surface atoms show a lower coordination number compared to their respective bulk atoms due to the missing of direct neighboring atoms. As an example, if for a bimetallic A–B nanoparticle system N_{A-M} is smaller than N_{B-M}, the A-type atoms are mainly located at the surface, while B-type atoms are positioned in the core of the nanoparticles. In our case, a preferred local enrichment of one single metal type within the nanochains of the aerogel framework was not observed for the Pd-rich Pd–Pt aerogels. Thus, the Pd and Pt atoms were distributed over the entire nanochains of the bimetallic aerogels.

The ratios of the partial coordination numbers (N_{Pd-Pt} and N_{Pt-Pd}) of the hetero-metallic Pd–Pt bond in the first shell can be used to establish the atomic ratios of Pt : Pd for the aerogels given in eqn (1). This relationship allows examining the local chemical environment of each element of the bimetallic aerogels.[39,40]

$$\frac{x_{Pt}}{x_{Pd}} = \frac{N_{Pd-Pt}}{N_{Pt-Pd}} \quad (1)$$

Table 1 First nearest neighbour coordination shell (N), atomic bond length (R), mean squared bond length disorder (σ^2), shift of energy (ΔE_0) at the corresponding edges, and R_f-factor (closeness of the fit as quality parameter) for all Pd–Pt aerogels

Aerogel	Bond	N	R/Å	$\sigma^2 \times 10^{-4}$/Å^2	ΔE_0/eV	R_f
$Pd_{80}Pt_{20}$	Pt–Pt_1	4.5 ± 1.2	2.720 ± 0.014	76 ± 20	6.3 ± 0.8	0.005
	Pt–Pd_1	5.5 ± 0.7	2.731 ± 0.008	73 ± 8		
	Pd–Pt_1	2.5 ± 0.6	2.731 ± 0.008	73 ± 8		
	Pd–Pd_1	7.3 ± 0.6	2.771 ± 0.005	85 ± 7	−9.1 ± 0.4	
$Pd_{60}Pt_{40}$	Pt–Pt_1	5.0 ± 0.8	2.739 ± 0.008	66 ± 10	7.4 ± 0.7	0.007
	Pt–Pd_1	4.0 ± 0.5	2.742 ± 0.007	77 ± 9		
	Pd–Pt_1	4.1 ± 0.7	2.742 ± 0.007	77 ± 9		
	Pd–Pd_1	5.7 ± 0.6	2.764 ± 0.006	77 ± 8	−8.1 ± 0.4	
$Pd_{50}Pt_{50}$	Pt–Pt_1	5.8 ± 0.6	2.737 ± 0.006	68 ± 7	7.0 ± 0.6	0.006
	Pt–Pd_1	2.9 ± 0.4	2.736 ± 0.007	73 ± 9		
	Pd–Pt_1	4.1 ± 0.8	2.736 ± 0.007	73 ± 9		
	Pd–Pd_1	5.8 ± 0.7	2.760 ± 0.007	73 ± 9	−10 ± 0.5	

Table 2 Chemical compositions obtained from EXAFS and EDX data, the total coordination numbers for Pt ($N_{Pt-M} = N_{Pt-Pt} + N_{Pt-Pd}$) and Pd ($N_{Pd-M} = N_{Pd-Pd} + N_{Pd-Pt}$) and the short range order parameter (α_{Pt-Pd} and α_{Pd-Pt}) for various Pd–Pt aerogels

Aerogel	First shell	N_{total}	x_{Pt}/x_{Pd} *via* EXAFS	x_{Pt}/x_{Pd} *via* EDX	α_{Pt-Pd}	α_{Pd-Pt}
$Pd_{80}Pt_{20}$	Pt–M	10.0 ± 0.9	0.5 ± 0.1	0.23 ± 0.01	+0.20	+0.18
	Pd–M	9.8 ± 0.6				
$Pd_{60}Pt_{40}$	Pt–M	9.0 ± 0.7	1.0 ± 0.1	0.59 ± 0.01	+0.10	+0.17
	Pd–M	9.8 ± 0.7				
$Pd_{50}Pt_{50}$	Pt–M	8.7 ± 0.5	2.0 ± 0.3	0.80 ± 0.01	0.00	+0.24
	Pd–M	9.9 ± 0.8				

Apart from EXAFS analysis, we used EDX as an independent bulk-averaging technique to determine the chemical composition of the aerogels over a broad length scale. Table 2 shows the direct comparison between the atomic ratios of Pt : Pd for all bimetallic aerogels established from both independent techniques. The atomic ratios of Pt : Pd *via* EXAFS significantly differed from those *via* EDX. Fig. 4b displays the atomic ratios of Pt : Pd for the as-prepared $Pd_{80}Pt_{20}$, $Pd_{60}Pt_{40}$ and $Pd_{50}Pt_{50}$ aerogels obtained from both analysis. As a guide to the eye, the dashed line in Fig. 4b symbolized the ideal case for identical results obtained from both techniques as used in this paper. In the case of homogeneous bimetallic alloy materials, identical results for the chemical composition are expected by the utilization of bulk-averaged techniques. Based on the EDX results (shown in Table 2), the measured atomic ratios of Pt : Pd are almost similar to the desired atomic Pt : Pd ratios adjusted during the synthesis. More specifically, the atomic ratios of Pt : Pd established by EDX were $Pt_{19\pm1}Pd_{81\pm1}$, $Pt_{37\pm1}Pd_{63\pm1}$ and $Pt_{44\pm1}Pd_{56\pm1}$ for the various Pd–Pt aerogels. The largest difference between the measured and the desired atomic ratios was observed for the $Pd_{50}Pt_{50}$ aerogel. Unlike EDX, the EXAFS results clearly revealed that the local chemical compositions of all Pd–Pt aerogels at around 2–3 Ångstrom strongly differed from the desired bulk chemical compositions. This observation signifies the features of chemical diversity and thus inhomogeneous distributions of both metals, Pd and Pt, in the macroscopic aerogel framework. The discrepancy between EXAFS and EDX can likely be explained by artifacts of EXAFS data analysis in particular for large disorder regions where the chemical composition changes from one location to the other.

Another useful descriptor to investigate the chemical environment of dissimilar atoms within bimetallic materials, the atomic arrangement of the involving atoms and the behaviors of clusters or alloys at the subnanometer-scale is the Cowley short range order parameter (α)[42–44] adapted to EXAFS analysis of bimetallic nanoalloys by Frenkel *et al.*[39–41] This parameter describes the relationship between the partial and total coordination numbers of the absorbing A-type atom in a bimetallic A–B system and is given by:

$$\alpha_A = 1 - \frac{N_{A-B}/N_{A-M}}{x_B} \quad (2)$$

where x_B is the molar concentration of B-type atoms, N_{A-B} is the partial coordination number of the A–B bond and N_{A-M} is the total coordination number of A-type atom ($N_{A-M} = N_{A-A} + N_{A-B}$). The molar concentration (x_B) is associated with the measured concentration in a local environment of the bimetallic material at the Ångstrom-scale and can be expressed by eqn (1). Depending on the mixing pattern of elements in the alloy, the short range order parameter α ranges from negative (for alloys with negative tendency to clustering of like atoms) to positive (for alloys with positive tendency to clustering) and is generally found between −1 and +1 for two dimensional bimetallic systems, where zero value corresponds to random mixing. The lowest possible α value in three-dimensional intermetallic fcc systems is −1/3.

To examine the chemical homogeneity and the local arrangement of the Pd and Pt atoms in all Pd–Pt aerogels at the Ångstrom-scale, we determined the short range order parameters of the Pt and Pd atoms (α_{Pt-Pd} and α_{Pd-Pt}) obtained from the multi-edge EXAFS fit analysis of both edge spectra. Table 2 shows the resulting short range order parameters (α_{Pt-Pd} and α_{Pd-Pt}) of all Pd–Pt aerogels being +0.1 for α_{Pt-Pd} and +0.2 for α_{Pd-Pt} for each Pd–Pt aerogel studied.

We suggest that the slightly positive value of the short range order parameter is likely related to the variation of the chemical composition along the nanochains of the bimetallic aerogel. Thus, the Pd–Pt aerogels prepared by the spontaneous one-step

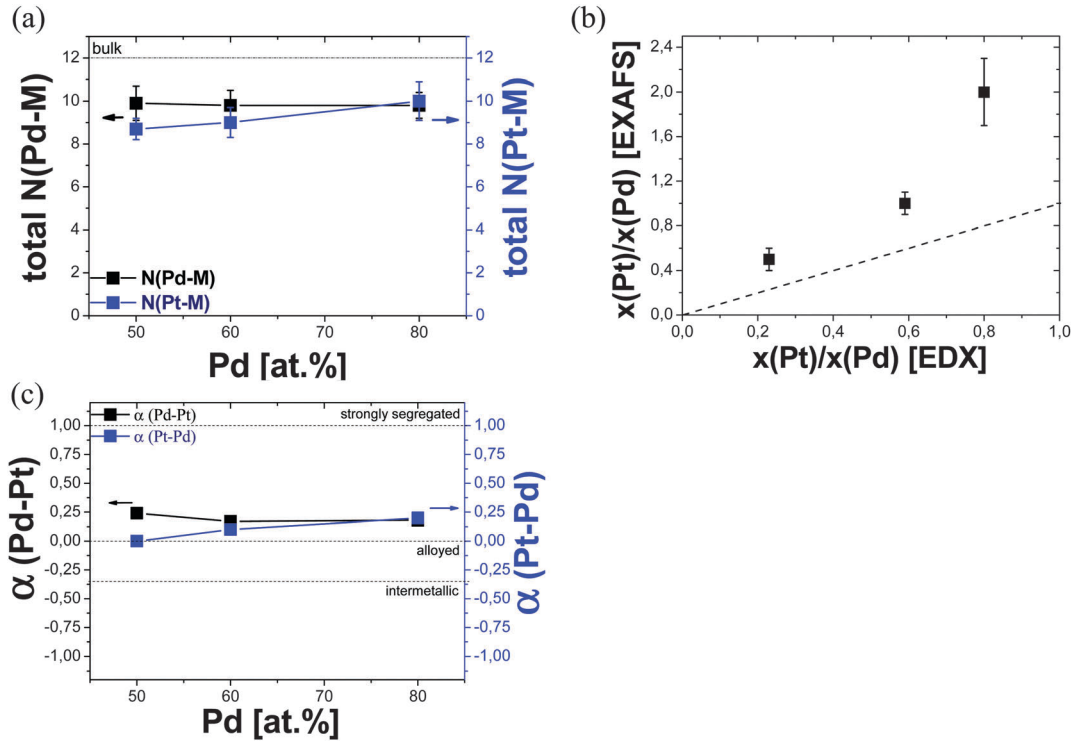

Fig. 4 (a) Total coordination numbers (N_{Pt-M} and N_{Pd-M}) *versus* aerogel composition. (b) Chemical compositions obtained from EXAFS and EDX analysis. The dashed lines visualize the ideal mixture of a bimetallic system. (c) Short range order parameter (α_{Pt-Pd} and α_{Pd-Pt}) in dependence of the content of Pd for the pristine Pd–Pt aerogels. Dashed lines symbolize the possible 3D-architectures of bimetallic systems such as intermetallic fcc motifs for $\alpha = -1/3$, randomly disordered alloyed motifs for $\alpha = 0$ and strongly segregated motifs for $\alpha = +1$.

gelation process form a randomly disordered alloy, where the chemical composition of the alloy varied from location-to-location along the nanochains. This variation in chemical composition is also indicated by slightly positive values of the short range order parameter (α_{Pt-Pd} and α_{Pd-Pt}).

In summary, the evaluation of the descriptors like total coordination numbers (N_{Pt-M} and N_{Pd-M}), atomic ratios of Pt : Pd based on the respective partial coordination numbers of the hetero-metallic Pd–Pt bond and short range order parameters (α_{Pt-Pd} and α_{Pd-Pt}) provide a detailed insight into the atomic arrangement and homogeneity of the $Pd_{80}Pt_{20}$, $Pd_{60}Pt_{40}$ and $Pd_{50}Pt_{50}$ aerogels at the subnanometer-scale. We showed that in the subnanometer range both metal atoms were well distributed and formed a randomly disordered alloy. The variation of the atomic ratios obtained from two independent techniques (EXAFS and EDX) can likely be related to the chemical diversity and thus inhomogeneous distributions of both metals, Pd and Pt, inside the entire aerogel framework.

3.1.4 Scanning transmission electron microscopy equipped with energy-dispersive X-ray spectroscopy (STEM-EDX). STEM-EDX investigations were performed to investigate the chemical distribution and homogeneity of the bimetallic aerogels at the few nm scale. As an example, a bright-field STEM micrograph of a representative region of nanochains for the $Pd_{50}Pt_{50}$ aerogel is shown in Fig. 5a. It is obvious that the nanochains are well connected with each other and form a three-dimensional porous structure. EDX maps were collected from this region of the $Pd_{50}Pt_{50}$ aerogel to uncover the elemental distribution of both metals within the nanochains. For the $Pd_{50}Pt_{50}$ aerogel, the measured EDX maps of the Pt L_α- and Pd L_α-lines are shown in Fig. 5b and c. The EDX maps for the Pt and Pd revealed that both metals are randomly arranged within the nanochains of the $Pd_{50}Pt_{50}$ aerogel at the resolution of this technique.

By overlapping of the single Pt and Pd EDX maps, it becomes clear that a strong enrichment of one metal along the nanochains took place, indicating a chemical heterogeneity inside the $Pd_{50}Pt_{50}$ aerogel. The chemical composition strongly varied from one location to the other along the nanochains. The observed Pt- or Pd-enriched regions are randomly distributed over the entire structure, signifying no preferred formation, growth or arrangement of the bimetallic nanochains during the gelation process. We observed that the Pd- or Pt-rich regions appear along the unbranched nanochains as well as at the cross-linked regions. The precise atomic ratios of Pd : Pt in a certain region of the nanowires were established by using EDX area analysis on quantified EDX maps (qmaps) of the investigated aerogel. Along the nanowires, several areas were chosen on the pristine $Pd_{50}Pt_{50}$ aerogel. The chemical results are illustrated in Fig. 5c. As a guide to the eye, the measured few nm-sized areas *via* EDX were denoted with white circles in the EDX map. It is obvious that the Pd content in this nanochain-segment of the macroscopic aerogel varied between 33 at% and 92 at%. Consequently, in the same area the Pt content ranged from 67 at% to 8 at%.

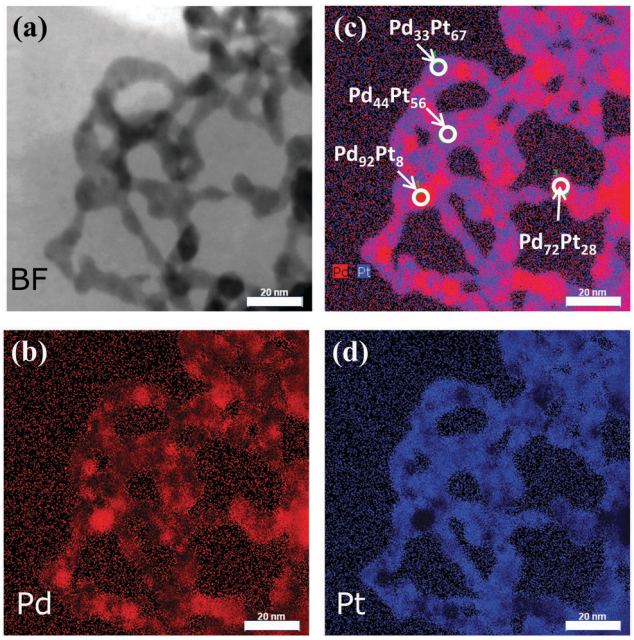

Fig. 5 Bright-field STEM micrograph (a) and the corresponding EDX maps for Pd (b) and Pt (d) measured from this region for the $Pd_{50}Pt_{50}$ aerogel. (c) Overlap of the EDX maps for each element. Pd and Pt are denoted with red and blue colors, respectively. The scale bar is 20 nm.

In summary, the STEM-EDX investigations on the $Pd_{50}Pt_{50}$ aerogel revealed that Pt and Pd atoms exist as a mixture inside the nanochains and that the chemical composition strongly varied from one location to the other. Both phenomena were independently confirmed by the EXAFS investigations.

3.2 Postulated structure and chemical distribution of Pd and Pt within the Pd-rich Pd–Pt aerogels

Based on the microscopic and spectroscopic results, we postulate the following structure and chemical distribution of the Pd and Pt atoms within the Pd-rich Pd–Pt aerogels. Fig. 6 illustrates a motif of the three-dimensional aerogel framework with variation of chemical composition along the nanochains and inside a nanoparticle being expressed as changing intensity and brightness of the purple color. No monometallic clusters or domains were detected by EXAFS or STEM-EDX. The Pd and Pt atoms are well distributed within the nanochains and form a randomly disordered alloy. However, the alloy composition varies from location to location along the nanochains and likely inside the nanoparticles over a broad length scale and form alloy phases with different chemical compositions. At the moment, it is rather difficult to examine the length scale of a nanochain segment with only one single alloy composition. As the chemical composition and structure of these materials strongly influence their reactivity, selectivity and durability in any heterogeneous and electrochemical reactions, a better understanding of the gelation process for the preparation of a homogeneous multi-metallic aerogel framework is necessary. In particular, effects of the mass transport of the monomers and kinetics of the reduction processes of dissimilar metals need to be investigated for the formation of the hydrogel.

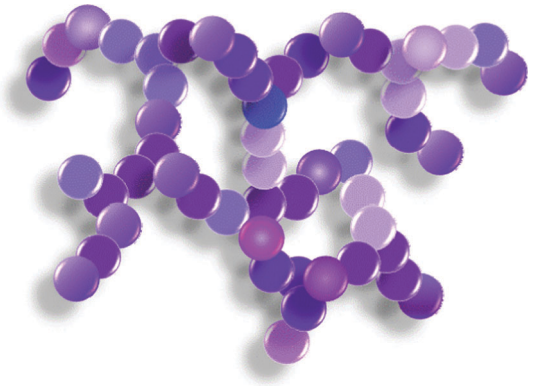

Fig. 6 Illustration of the structure and chemical distribution of the Pd-rich Pd–Pt aerogels prepared by the spontaneous one-step gelation process. The strong variation of the alloy composition in the Pd–Pt aerogels is symbolized by changing the intensity and brightness of the purple color.

3.3 Electrochemically active surface area (ECSA) investigations of the Pd–Pt aerogels

In Fig. 7a, the CV profiles for all Pd–Pt aerogels clearly show the electrochemical oxidation of a monolayer of the adsorbed CO (CO_{ML}) at the aerogel surface during the anodic scan. Only one CO oxidation current peak was detected in the CV profiles for each bimetallic aerogel. It is visible that the positions of the three maxima of the CO stripping peaks appear at significantly different potentials. As deduced from Fig. 7a, the anodic peak potentials were 0.79, 0.81 and 0.87 V per RHE for $Pd_{50}Pt_{50}$, $Pd_{60}Pt_{40}$ and $Pd_{80}Pt_{20}$, respectively. Since the mean particle size and the total coordination numbers obtained from TEM and EXAFS investigations for all Pd–Pt aerogels are similar, an effect of the particle size can be excluded, see the previous section. Therefore, the shift of the CO stripping current peak is likely related to the chemical composition at the surface and subsurface of the aerogels. Similar results were observed by Feliu and coworkers.[45,46] They prepared different coverages of Pd as a monolayer on a Pt single crystal and showed that the potential of the CO stripping peak moved to higher positive values by increasing the coverage of Pd at the surface. This observation was explained by the lower reactivity of Pd for the CO oxidation compared to Pt. The variation of the reactivity for Pd and Pt is attributed to the different bond strengths of CO_{ads} and/or bond strengths of OH_{ads}.[47,48] Since only one CO stripping peak was observed for each aerogel, discrimination between Pd and Pt surface atoms is impossible. Therefore, the resulting values of ECSA obtained from the integration of the CO stripping current peak correspond to the used total content of metal (Pd and Pt). In other words, the experimentally observed surface areas for all bimetallic aerogels were normalized by the total metal content. The resulting values of ECSA for the various Pd–Pt aerogels are summarized in Fig. 7b. The values of ECSA are 33 ± 1, 46 ± 4 and 43 ± 3 m^2 $g_{(Pd+Pt)}^{-1}$ for the $Pd_{80}Pt_{20}$, $Pd_{60}Pt_{40}$ and $Pd_{50}Pt_{50}$ aerogels, respectively. For comparison, we chose a commercially available unsupported Pt black catalyst (ECSA = 16 ± 2 m^2 g_{Pt}^{-1}). It is noted that the experimentally observed ECSA clearly differed from the measured BET values for all

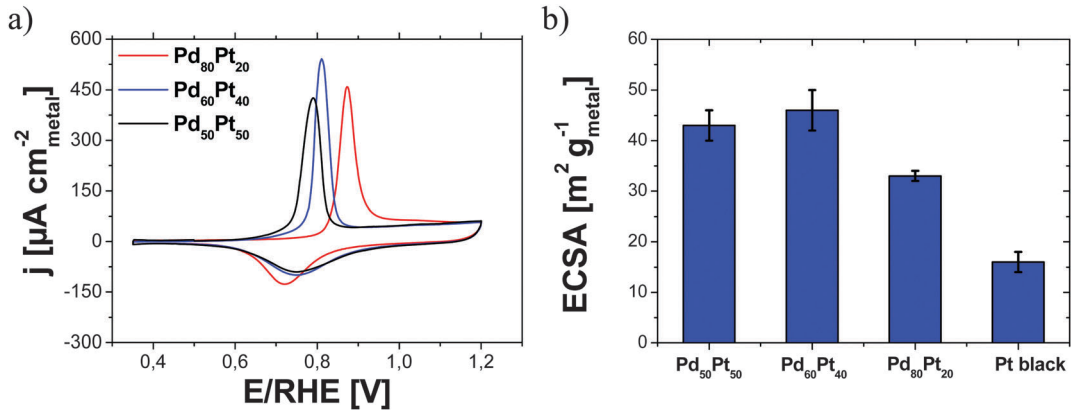

Fig. 7 (a) CO stripping cyclic voltammetry (CV) profiles of the $Pd_{80}Pt_{20}$ (red line), $Pd_{60}Pt_{40}$ (blue line) and $Pd_{50}Pt_{50}$ (black line) aerogels. Experimental parameters: scan rate of 50 mV s^{-1}, metal loading of 12–17 μg $cm_{(geo.)}^{-2}$ in 0.1 M $HClO_4$ at room temperature. (b) Comparison between the values of the electrochemically active surface area (ECSA) for various Pd–Pt aerogels and the commercially available unsupported Pt black catalyst.

Pd–Pt aerogels of 60–80 m^2 g^{-1}.[3] The large discrepancy between the two measurements (BET *vs.* CO stripping) is likely an effect of accessibility/wettability restrictions in the micro-pores of the aerogels or effects of surface oxides and impurities like strongly adsorbed anions from the synthesis.

Further strategies are required to increase the ECSA for the Pd–Pt aerogels as the experimentally observed values of ECSA are not as high as known for commercially available Pt nanoparticles supported on high surface area carbon materials (60 to 90 m^2 g_{Pt}^{-1} [17,49,50]).

4. Conclusions

Bimetallic Pd–Pt aerogels with three different chemical compositions were prepared by the spontaneous one-step gelation process. We used different independent techniques, EXAFS and STEM-EDX, to analyze in detail the structure and chemical composition of the pristine $Pd_{80}Pt_{20}$, $Pd_{60}Pt_{40}$ and $Pd_{50}Pt_{50}$ aerogels at different relevant length scales. In particular, the evaluation of the partial coordination numbers, the total coordination numbers and the short range order parameters established from EXAFS provides insights into the chemical distribution of the various Pd–Pt aerogels at the Ångstrom-scale. Based on the EXAFS and STEM-EDX results, we can conclude that all Pd–Pt aerogels largely showed a characteristic alloying behavior inside the nanochains. The appearance of an alloyed phase for the Pd–Pt aerogels was established by the partial coordination numbers of Pd–Pt bonds in the first coordination shell of 2–3 Å. The EXAFS and STEM-EDX results also signified the inhomogeneity of these materials on the larger scale by the appearance of strong variation of the chemical composition along the nanochains. We also studied the electrochemically active surface area (ECSA) of the Pd–Pt aerogels by using the electrochemical CO stripping method. The Pd–Pt aerogels showed 2–2.8 times higher ECSA compared to a commercially available unsupported Pt black catalyst. However, the comparison between ECSA and BET surface area revealed that the surfaces of the Pd–Pt aerogels are not entirely accessible for the electrocatalytic applications. The observed large difference is likely based on wettability restrictions within the micro-pores, and/or the presence of surface oxides and impurities.

Therefore, a better understanding of the gelation process will help to design homogeneous bimetallic aerogels with improved activity and durability for fuel cell application. Further work is planned to investigate the structure and chemical homogeneity of Pt-rich Pd–Pt aerogels. Although the alloying of both metals in self-assembled macroscopic aerogels was realized by this synthetic method, the chemical homogeneity over a broad length scale and the accessibility of the surface need to further improve. The possible strategies for the preparation of homogeneous bimetallic aerogels can be a better reactant mass transport process during synthesis and a careful adjustment of the reducing agents during the gelation process.

Acknowledgements

Financial support from the Deutsche Forschungsgemeinschaft (DFG), the Swiss National Science Foundation (SNF), the European Research Council (ERC-2013-AdG AEROCAT) and the Bundesministerium für Bildung und Forschung (BMBF, 03SF0539) is gratefully acknowledged. A. I. F. acknowledges funding of his work by the U. S. Department of Energy Grant No. DE-FG02-03ER15476. The research leading to the STEM-HAADF and STEM-EDX results has received funding from the European Union Seventh Frame-work Program under Grant Agreement 312483 – ESTEEM2 (Integrated Infrastructure Initiative-I3). The authors thank the Swiss Light Source for the provision of beamtime at the SuperXAS beamline.

References

1 W. Liu, A.-K. Herrmann, N. C. Bigall, P. Rodriguez, D. Wen, M. Oezaslan, T. J. Schmidt, N. Gaponik and A. Eychmüller, *Acc. Chem. Res.*, 2015, **48**, 154–162.
2 W. Liu, A.-K. Herrmann, D. Geiger, L. Borchardt, F. Simon, S. Kaskel, N. Gaponik and A. Eychmüller, *Angew. Chem., Int. Ed.*, 2012, **51**, 5743–5747.

3 W. Liu, P. Rodriguez, L. Borchardt, A. Foelske, J. Yuan, A.-K. Herrmann, D. Geiger, Z. Zheng, S. Kaskel, N. Gaponik, R. Kötz, T. J. Schmidt and A. Eychmüller, *Angew. Chem., Int. Ed.*, 2013, **52**, 9849–9852.
4 A.-K. Herrmann, P. Formanek, L. Borchardt, M. Klose, L. Giebeler, J. Eckert, S. Kaskel, N. Gaponik and A. Eychmüller, *Chem. Mater.*, 2014, **26**, 1074–1083.
5 Y. Xu and B. Zhang, *Chem. Soc. Rev.*, 2014, **43**, 2439–2450.
6 P. Trogadas, V. Ramani, P. Strasser, T. F. Fuller and M.-O. Coppens, *Angew. Chem., Int. Ed.*, 2016, **55**, 122–148.
7 M. Shao, Q. Chang, J.-P. Dodelet and R. Chenitz, *Chem. Rev.*, 2016, **116**, 3594–3657.
8 C. Zhu, D. Du, A. Eychmüller and Y. Lin, *Chem. Rev.*, 2015, **115**, 8896–8943.
9 H. D. Gesser and P. C. Goswami, *Chem. Rev.*, 1989, **89**, 765–788.
10 N. Hüsing and U. Schubert, *Angew. Chem., Int. Ed.*, 1998, **37**, 22–45.
11 L. Liu, L.-X. Chen, A.-J. Wang, J. Yuan, L. Shen and J.-J. Feng, *Int. J. Hydrogen Energy*, 2016, **41**, 8871–8880.
12 M. Oezaslan, F. Hasché and P. Strasser, *J. Phys. Chem. Lett.*, 2013, **4**, 3273–3291.
13 V. R. Stamenkovic, B. Fowler, B. S. Mun, G. Wang, P. N. Ross, C. A. Lucas and N. M. Markovic, *Science*, 2007, **315**, 493–497.
14 C. Chen, Y. Kang, Z. Huo, Z. Zhu, W. Huang, H. L. Xin, J. D. Snyder, D. Li, J. A. Herron, M. Mavrikakis, M. Chi, K. L. More, Y. Li, N. M. Markovic, G. A. Somorjai, P. Yang and V. R. Stamenkovic, *Science*, 2014, **343**, 1339–1343.
15 C. Koenigsmann, A. C. Santulli, K. Gong, M. B. Vukmirovic, W.-p. Zhou, E. Sutter, S. S. Wong and R. R. Adzic, *J. Am. Chem. Soc.*, 2011, **133**, 9783–9795.
16 M. J. Byungkwon Lim, P. H. C. Camargo, E. C. Cho, J. Tao, X. Lu, Y. Zhu and Y. Xia, *Science*, 2009, **324**, 1302–1305.
17 H. A. Gasteiger, S. S. Kocha, B. Sompalli and F. T. Wagner, *Appl. Catal., B*, 2005, **56**, 9–35.
18 H. A. Gasteiger and N. M. Markovic, *Science*, 2009, **324**, 48–49.
19 M. K. Debe, *Nature*, 2012, **486**, 43–51.
20 I. Chorkendorff, I. E. L. Stephens, A. S. Bondarenko, U. G. Andersen and J. Rossmeisl, *Energy Environ. Sci.*, 2012, **5**, 6744–6762.
21 A. Rabis, P. Rodriguez and T. J. Schmidt, *ACS Catal.*, 2012, **2**, 864–890.
22 F. Hasché, M. Oezaslan and P. Strasser, *ChemCatChem*, 2011, **3**, 1805–1813.
23 M. Oezaslan and P. Strasser, *J. Power Sources*, 2011, **196**, 5240–5249.
24 T. Toda, H. Igarashi and M. Watanabe, *J. Electrochem. Soc.*, 1998, **145**, 4185–4188.
25 T. Toda, H. Igarashi, H. Uchida and M. Watanabe, *J. Electrochem. Soc.*, 1999, **146**, 3750–3756.
26 S. Mukerjee and S. Srinivasan, *J. Electroanal. Chem.*, 1993, **357**, 201–224.
27 V. Stamenkovic, T. J. Schmidt, P. N. Ross and N. M. Markovic, *J. Phys. Chem. B*, 2002, **106**, 11970–11979.
28 D. A. Slanac, W. G. Hardin, K. P. Johnston and K. J. Stevenson, *J. Am. Chem. Soc.*, 2012, **134**, 9812–9819.
29 J. R. Kitchin, J. K. Norskov, M. A. Barteau and J. G. Chen, *Phys. Rev. Lett.*, 2004, **93**, 156801.
30 J. R. Kitchin, J. K. Nørskov, M. A. Barteau and J. G. Chen, *J. Chem. Phys.*, 2004, **120**, 10240–10246.
31 S. Yun and S. Ted Oyama, *J. Membr. Sci.*, 2011, **375**, 28–45.
32 M. G. Montes de Oca, H. Kumarakuru, D. Cherns and D. J. Fermín, *J. Phys. Chem. C*, 2011, **115**, 10489–10496.
33 M. Newville, *J. Synchrotron Radiat.*, 2001, **8**, 322–324.
34 T. J. Schmidt, H. A. Gasteiger, G. D. Stab, P. M. Urban, D. M. Kolb and R. J. Behm, *J. Electrochem. Soc.*, 1998, **145**, 2354–2358.
35 T. J. Schmidt and H. A. Gasteiger, in *Handbook of Fuel Cells – Fundamentals, Technology, and Applications*, ed. W. Vielstich, A. Lamm and H. Gasteiger, Wiley, Chichester, 2003, ch. 322, p. 316.
36 F. Maillard, E. R. Savinova and U. Stimming, *J. Electroanal. Chem.*, 2007, **599**, 221–232.
37 M. Hara, U. Linke and T. Wandlowski, *Electrochim. Acta*, 2007, **52**, 5733–5748.
38 ICDD, International Center for Diffraction Data – Power Diffraction File (PDF) 2 data CD http://www.icdd.com/, 2002.
39 A. I. Frenkel, A. Yevick, C. Cooper and R. Vasic, *Annu. Rev. Anal. Chem.*, 2011, **4**, 23–39.
40 A. I. Frenkel, Q. Wang, S. I. Sanchez, M. W. Small and R. G. Nuzzo, *J. Chem. Phys.*, 2013, **138**, 064202.
41 A. I. Frenkel, *Chem. Soc. Rev.*, 2012, **41**, 8163–8178.
42 J. M. Cowley, *Phys. Rev.*, 1965, **138**, A1384–A1389.
43 J. M. Cowley, *Phys. Rev.*, 1960, **120**, 1648–1657.
44 J. M. Cowley, *Phys. Rev.*, 1950, **77**, 669–675.
45 B. Álvarez, A. Berná, A. Rodes and J. M. Feliu, *Surf. Sci.*, 2004, **573**, 32–46.
46 B. Álvarez, V. Climent, A. Rodes and J. M. Feliu, *J. Electroanal. Chem.*, 2001, **497**, 125–138.
47 B. Hammer, Y. Morikawa and J. K. Norskov, *Phys. Rev. Lett.*, 1996, **76**, 2141–2144.
48 F. Hanne, H. Britt, S. K. Iben, J. Tao, B. Thomas, H. C. Claus and K. N. Jens, *Angew. Chem.*, 2008, **120**, 4913–4917.
49 F. Hasché, M. Oezaslan and P. Strasser, *Phys. Chem. Chem. Phys.*, 2010, **12**, 15251–15258.
50 M. Nesselberger, S. Ashton, J. C. Meier, I. Katsounaros, K. J. J. Mayrhofer and M. Arenz, *J. Am. Chem. Soc.*, 2011, **133**, 17428–17433.